Graphene-templated synthesis of sandwich-like porous carbon nanosheets for efficient oxygen reduction reaction in both alkaline and acidic media

Tao Wang[1], Jianyu Wang[2], Xu Wang[1], Jia Yang[1], Jianguo Liu[2*] and Hangxun Xu[1*]

ABSTRACT   **Developing low-cost, high-performance electrocatalysts for the oxygen reduction reaction (ORR) is crucial for implementation of fuel cells and metal-air batteries into practical applications. Graphene-based catalysts have been extensively investigated for ORR in alkaline electrolytes. However, their performance in acidic electrolytes still requires further improvement compared to the Pt/C catalyst. Here we report a self-templating approach to prepare graphene-based sandwich-like porous carbon nanosheets for efficient ORR in both alkaline and acidic electrolytes. Graphene oxides were first used to adsorb *m*-phenylenediamine molecules which can form a nitrogen-rich polymer network after oxidative polymerization. Then iron (Fe) salt was introduced into the polymer network and transformed into ORR active Fe–N–C sites along with Fe, FeS, and $FeN_{0.05}$ nanoparticles after pyrolysis, generating ORR active sandwich-like carbon nanosheets. Due to the presence of multiple ORR active sites. The as-obtained catalyst exhibited prominent ORR activity with a half-wave potential ~30 mV more positive than Pt/C in 0.1 mol L^{-1} KOH, while the half-wave potential of the catalyst was only ~40 mV lower than that of commercial Pt/C in 0.1 mol L^{-1} $HClO_4$. The unique planar sandwich-like structure could expose abundant active sites for ORR. Meanwhile, the graphene layer and porous structure could simultaneously enhance electrical conductivity and facilitate mass transport. The prominent electrocatalytic activity and durability in both alkaline and acidic electrolytes indicate that these carbon nanosheets hold great potential as alternatives to precious metal-based catalysts, as demonstrated in zinc-air batteries and proton exchange membrane fuel cells.**

Keywords: oxygen reduction reaction, porous carbon, nanosheets, fuel cells, zinc-air batteries

INTRODUCTION

With the emerging global energy crisis and the growing environmental concerns, the development of efficient and renewable energy conversion and storage devices has become a critically important research topic. Fuel cells and metal-air batteries are two of the most promising electrochemical energy conversion devices with high energy utilization and safety [1–5]. However, the lack of efficient and low-cost electrocatalysts toward oxygen reduction reaction (ORR) occurring at the cathodes of fuel cells and metal-air batteries impedes the implementation of metal-air batteries and fuel cells in practical applications [6–10]. Although Pt-based precious metal catalysts possess the most intriguing catalytic performance in prototype devices, the high cost associated with poor durability is a severe issue preventing their further development [11,12]. Therefore, it is urgent to develop alternative non-precious metal catalysts (NPMCs) with high electrocatalytic activity and long-term stability to promote the commercialization of metal-air batteries and fuel cells in the near future [13–19].

Recently, NPMCs containing transition meal-nitrogen-carbon (M–N–C, M=Fe, Co) sites have attracted considerable attention due to their prominent catalytic performance in alkaline media [18–24]. In particular, Fe/N-doped carbon electrocatalysts have been considered as a very promising family of NPMCs for ORR because of the high catalytic activity, easy access, and cheap iron resources [24–32]. However, the ORR activity of Fe–N–C catalysts still remains deficient compared to that of Pt-based catalysts in acidic media, owing to the low density of active sites [33–38]. Meanwhile, the specific surface

[1] CAS Key Laboratory of Soft Matter Chemistry, Department of Polymer Science and Engineering, University of Science and Technology of China, Hefei 230026, China
[2] National Laboratory of Solid State Microstructures, College of Engineering and Applied Sciences, Collaborative Innovation Center of Advanced Microstructures, Nanjing University, Nanjing 210093, China
* Corresponding authors (emails: hxu@ustc.edu.cn (Xu H); jianguoliu@nju.edu.cn (Liu J))

area and porous structure of carbon-based NPMCs have influence on the accessibility of the active sites and ORR activity [39–43]. Consequently, rational design of porous carbon structures with abundant Fe-N-C active sites is highly desired. In this context, graphene is a very intriguing candidate for constructing two-dimensional (2D) porous NPMCs [44,45]. The 2D planar nature would be beneficial for exposing active sites on the surface and transporting/exchanging ORR-relevant species [46]. Moreover, the highly conductive nature of graphene could further facilitate charge transfer during ORR [47]. Nonetheless, metal species are difficult to be directly doped into pure graphene due to the lack of strong bonding between metal species and graphene. Due to strong coordination with amines of metal ions, it is a potentially viable approach that a layer of nitrogen-rich polymer with multiple coordination sites for metal species which can then be transformed into M-N-C sites after pyrolysis is coated on the surface of graphene [48–50].

Herein, we report the graphene-templated synthesis of sandwich-like porous carbon nanosheets in which each graphene nanosheet is encapsulated by a porous carbon shell with multiple dopants (i.e., N, S, and Fe–N) and embedded nanoparticles (i.e., Fe, FeS, and $FeN_{0.05}$). Crosslinked poly(*m*-phenylenediamine) (P*m*PDA) layer was initially formed on graphene oxides (GO) as nitrogen sources and anchoring sites for Fe^{3+} ions. After adsorption and pyrolysis of Fe^{3+} ions, porous carbon nanosheets with a high surface area (1105 m^2 g^{-1}) can be obtained (hereafter referred to as the P*m*PDA-GR-Fe catalyst). P*m*PDA contains more nitrogen content than polyaniline and polypyrrole, which can provide more nitrogen sources and coordination sites for Fe and thus could potentially enhance the electrocatalytic performance. In addition to N-doping, S could also be introduced into the carbon nanosheets during the oxidative polymerization process by using ammonium persulfate (APS) as the oxidant. In this way, the doping step is simplified while the element utilization efficiency is improved. Moreover, the existence of nanoparticles such as Fe, FeS, and $FeN_{0.05}$ could further boost the ORR activity by tuning the redox properties of surrounding carbon layers embedded with active sites [51]. Consequently, the resulting P*m*PDA-GR-Fe catalyst exhibited prominent ORR activity as well as excellent long-term stability both in alkaline and acidic media, surpassing those of commercial Pt/C catalyst (20 wt% Pt, Johnson Matthey). To assess the potential of this ORR catalyst for practical applications, the P*m*PDA-GR-Fe catalyst was further assembled as cathodes for a zinc-

air battery and a proton exchange membrane fuel cell (PEMFC), respectively. Both results indicated that the P*m*PDA-GR-Fe catalyst exhibited excellent ORR activity in real electrochemical devices, suggesting that the reported catalyst is very promising for practical applications.

EXPERIMENTAL SECTION

Synthetic procedures

In a typical synthesis, 1 g *m*-phenylenediamine (*m*PDA) dissolved in 30 mL 1 mol L^{-1} HCl solution was mixted with a 50 mL GO solution containing 45 mg GO. Meanwhile, 4 g ammonium persulfate (APS) was dissolved in 50 mL 1 mol L^{-1} HCl solution. Both solutions were cooled to 4°C. Then, the APS solution was slowly added to the mixed *m*PDA/GO solution with vigorous stirring. After reaction for 8 h, the dark colored product was washed to be neutral with water several times. Finally, dried P*m*PDA-GO powder was obtained after vacuum drying for 12 h at 80°C. The dry powder of P*m*PDA-GO (0.1 g) was added into a 0.08 mol L^{-1} Fe $(NO_3)_3$ solution. After ~24 h, the solvent was removed using a rotary evaporator. Then, the resulting powder was heated at 900°C under N_2 atmosphere for 2 h. Subsequently, the pyrolyzed sample was added into 1 mol L^{-1} HCl solution at 80°C for 12 h followed by centrifugation and washing with deionized water. This step was performed to remove electrochemically inactive and unstable species. Finally, the obtained powder was pyrolyzed at the same temperature for 2 h, leading to the final catalyst denoted as P*m*PDA-GR-Fe.

Materials characterization

Scanning electron microscopy (SEM) was performed on a FEI SIRION200 microscope. High-resolution transmission electron microscopy (HRTEM) was conducted on a JEM-ARM 200F Atomic Resolution Analytical Microscope operating at an accelerating voltage of 200 kV. Powder X-ray diffraction (PXRD) patterns were obtained using a Japan Rigaku DMax-γA rotation anode X-ray diffractometer. The N_2 adsorption-desorption experiments were carried out using the Belsorp-max instrument. X-ray photoelectron spectroscopy (XPS) measurements were performed on an X-ray photoelectron spectrometer (Thermo ESCALAB 250).

Electrochemical measurements

All electrochemical measurements were performed in a

three-electrode system using a PGSTAT302N electro-chemical workstation (Metrohm Autolab) at room temperature. A 5.0 mm glassy carbon rotating disk electrode (PINE Research Instrumentation, USA) served as the substrate for working electrode. A platinum sheet and saturated calomel electrode served as the counter and reference electrodes, respectively. The reference electrode was calibrated with respect to reversible hydrogen electrode (RHE) before each experiment. The glassy carbon electrode was thoroughly cleaned before each test. To prepare the working electrode, 2 mg of the catalyst was dispersed in 1 mL ethanol and sonicated to get a homogeneous ink, followed by adding 10 μL 5% Nafion solution. Then, the catalyst ink was drop-casted on the glassy carbon electrode and dried at room temperature (catalyst loading: ~0.2 mg cm^{-2} in alkline media, ~0.4 mg cm^{-2} in acidic media).

For ORR measurements, the cyclic voltammetry (CV) experiments were performed in Ar/O_2 saturated 0.1 mol L^{-1} KOH and 0.1 mol L^{-1} HClO$_4$ at room temperature with a scan rate of 10 mV s^{-1}. Rotating disk electrode (RDE) tests were performed in O_2 saturated 0.1 mol L^{-1} KOH and 0.1 mol L^{-1} HClO$_4$ with a scan rate of 10 mV s^{-1}. The electron transfer number during ORR was calculated by Koutecky-Levich equation. Rotating ring-disk electrode (RRDE) measurements were carried out to determine the four-electron selectivity according to the previous report [25].

Zinc-air battery and fuel cell tests
Zinc-air batteries were assembled in home-made cells. For example, a zinc-air battery was assembled by pairing the as-synthesized catalyst ink loaded on a porous carbon paper electrode (0.5 mg cm^{-2}) with a Zn foil in 6 mol L^{-1} KOH. PEMFC cathode catalyst was PmPDA-GR-Fe with a loading mass of 4 mg cm^{-2} or 60 wt% Pt/C from Johnson Matthey with a loading mass of 0.8 mg cm^{-2}. To enhance protonic conductivity, 60 wt% of Nafion content in cathode catalyst layer was used. The anode catalyst was 60 wt% Pt/C with a loading mass of 0.8 mg cm^{-2}, and the Nafion content in anodic catalyst layer was 30 wt%. The catalyst layer in the anode and the cathode was brushed on the gas diffusion layer (Sunrise Power Inc. China) based on Toray 060 carbon paper. Then, the membrane electrode assembly (MEA) was prepared by hot-pressing the electrodes and Nafion 211 membrane with an active area of 1.0 cm^2. Fuel cell polarization curve was tested at 80°C on a fuel cell test system (Model 850e, Scribner Associates Inc.). H_2 and O_2 flow rates were 300 mL min^{-1} at 100% RH, and no back pressure was applied (i.e., the
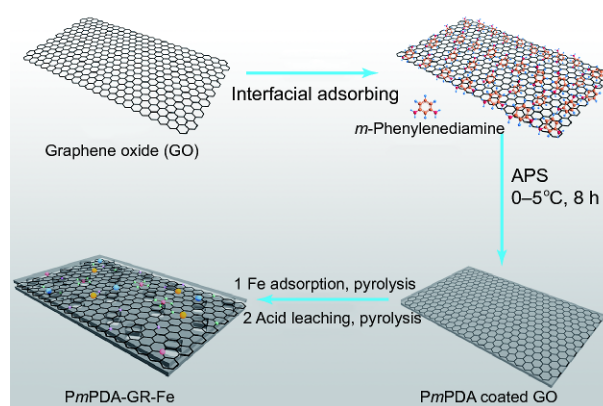

Scheme 1 Schematic illustration for the preparation of sandwich-like heteroatom-doped carbon nanosheets. Graphene oxides were first used as the template to adsorb m-PDA followed by an *in situ* polymerization process. Subsequently, after adsorbing Fe^{3+} ions, the polymer coated graphene oxides were subjected to pyrolysis and acid leaching, leading to the final PmPDA-GR-Fe catalyst.

O_2 and H_2 partial pressure was about 0.53 bar since the saturation water vapor pressure at 80°C is ca. 0.47 bar).

RESULTS AND DISSCUSIONS
The PmPDA-GR-Fe catalyst was prepared following the procedures schematically shown in Scheme 1. Briefly, m-PDA monomers were first adsorbed onto GO surface due to π–π interactions, hydrogen bonding and electrostatic interactions (Fig. S1). Subsequently, PmPDA layer was formed on GO surface by *in situ* polymerization using APS as the oxidant to yield the PmPDA-GO hybrid. As shown in Fig. S2, the thickness of the sheet-like structure is ~4 nm, indicating the PmPDA layer successfully coated on GO. PmPDA-GO was then mixed with proper amount of ferric nitrate solution for 24 h to introduce Fe species into the hybrid. After drying, the mixed sample was subjected to pyrolysis at 900°C in N$_2$ atmosphere for 2 h. The pyrolyzed product was leached in hot HCl solution to remove unstable and electrochemically inactive species. Finally, the leached sample was annealed under the same temperature for 2 h to afford the PmPDA-GR-Fe electrocatalyst with a sandwich-like structure.

The detailed microstructure was further examined by using SEM and transmission electron microscope (TEM). As shown in Fig. 1a and d, GO could successfully act as the template to form sheet-like structure by *in situ* polymerization mPDA monomers into PmPDA on the surface of GO. Meanwhile, the 2D sheet-like structure still retained after pyrolysis to yield PmPDA-GR (Fig. 1a, d). After introducing Fe into the polymer network, many visible pores and nanoparticles were formed after carbo-
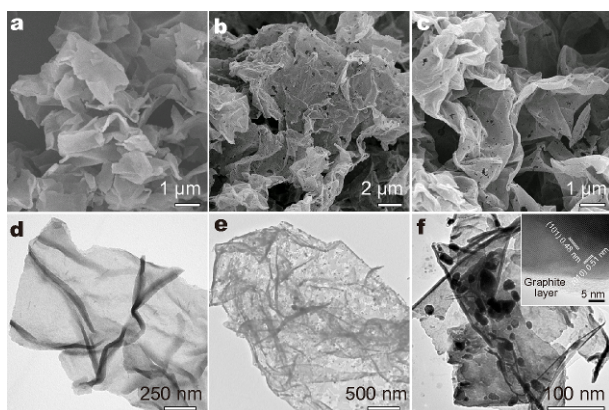
Figure 1 (a, d) SEM and TEM images of P*m*PDA-GR. (b, e) SEM and TEM images of P*m*PDA-GR-Fe before acid leaching. (c, f) SEM and TEM images of the final P*m*PDA-GR-Fe catalyst. The FeS nanoparticles encapsulated in graphitic carbons were identified with the index crystal plane displayed in the inset in (f).

Figure 2 HAADF-STEM image of the P*m*PDA-GR-Fe catalyst and the corresponding EDX elemental mapping images for C, Fe, O, N, and S elements.

nization (Fig. 1b, e). However, after acid leaching process, almost all of the visible nanoparticles that exposed to the outside of the nanosheets disappeared in P*m*PDA-GR-Fe and some large pores are clearly seen (Fig. 1c), suggesting that introducing Fe species is beneficial for the formation of porous structures. Although nanoparticles could not be observed in SEM image as shown in Fig. 1c, TEM image (Fig. 1f) clearly indicates the presence of nanoparticles with sizes of tens of nanometers in the final sandwich-like structure. The inset in Fig. 1f shows a typical nanoparticle with the spacing of the crystalline lattices in two directions, 0.48 and 0.51 nm, respectively, corresponding to (101) and (010) planes of the FeS phase [52]. Moreover, the crystalline carbon layer can be easily identified as the (002) plane of graphitic carbon with an interlayer spacing of 0.34 nm. The encapsulated FeS nanoparticles could activate the surrounding graphitic layers, making the outer carbon layers highly active toward ORR [53,54].

Elemental mapping results (Fig. 2) demonstrate that both C and N are uniformly distributed in the carbon nanosheets. The strong Fe element signals exist in the areas of nanoparticles, indicating the formation of Fe-based nanoparticles during pyrolysis. Meanwhile, S element was observed from the mapping results which also distributed over the carbon nanosheets. By comparing the Fe and S mapping images, we could find that there are other Fe-based nanoparticles other than FeS. As shown in powder X-ray diffraction (PXRD) patterns (Fig. 3a), the diffraction peaks can be assigned to the FeS, Fe, and FeN$_{0.05}$, which are consistent with the elemental mapping results. Raman spectra (Fig. S3) reveal the characteristic G and D bands of carbon, corresponding to the graphitic
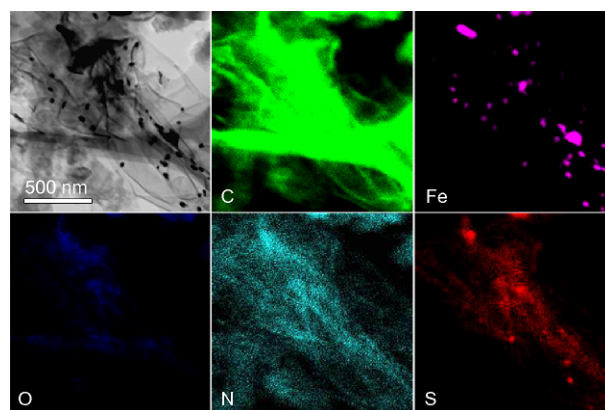
and disordered or defect carbons, respectively. Elemental analysis (EA) and inductively coupled plasma mass spectrometry (ICP-MS) indicated that the C, N, S, O, and Fe contents in P*m*PDA-GR-Fe were 88.42, 4.94, 1.31, 3.53, and 1.33 wt%. The steep increase in N$_2$ uptake at the low pressure region suggested the existence of abundant micropores. Brunauer-Emmett-Teller (BET) surface area of P*m*PDA-GR-Fe measured by N$_2$ sorption/desorption isotherms is 1,105 m^2 g^{-1} with an average pore size of ~0.54 nm (Fig. 3b). Compared to the sample before acid leaching, introducing Fe species into the P*m*PDA-GR-Fe could significantly improve the surface area and pore volume. The high specific surface area has been shown to be beneficial for promoting catalytic activity [55]. XPS revealed the presence of C (89.91 at%), N (3.94 at%), S (1.11 at%), O (4.66 at%), and Fe (0.48 at%) (Fig. S4a). The Fe content measured from XPS is lower than that obtained from ICP-MS (1.33 wt%), indicating that the Fe species are partially embedded within the sandwich-like structure. The high-resolution N 1s spectrum (Fig. S4b) can be deconvoluted into several peaks at 398.5, 399.5, 400.3, 401.3, and 403.9 eV, which can be assigned to pyridinic N (24.3%), Fe–N (4.6%), terminal graphitic N (10.3%), central graphitic N (54.1%) and oxidized N (6.7%), respectively [28]. The high content of pyridinic and graphitic N which are also identified in the X-ray near-edge structure spectrum of N K-edge (XANES, Fig. S5a) should be beneficial for ORR [56,57]. The S 2p spectrum of P*m*PDA-GR-Fe can be fitted into three peaks (Fig. 3c). Two major peaks at 163.9 and 165.0 eV are assigned to S 2p$_{3/2}$ and S 2p$_{1/2}$ peaks for the –C–S–C– covalent bond of thiophene-type sulfur owning to the spin-orbit splitting [58]. The remaining peak belongs to the oxidized S. The –C–S–C– configuration was also
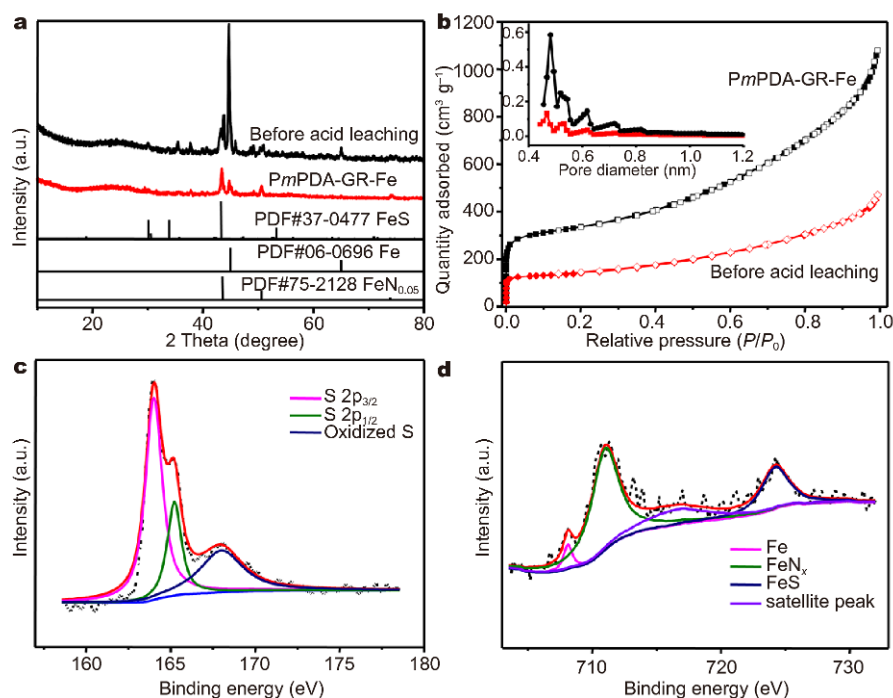
Figure 3 (a) PXRD patterns of P*m*PDA-GR-Fe before and after acid leaching. (b) N_2 adsorption-desorption isotherms and corresponding pore size distribution (inset) of P*m*PDA-GR-Fe before and after acid leaching. Deconvoluted XPS spectra of (c) S 2p and (d) Fe 2p peaks for the P*m*PDA-GR-Fe catalyst.

confirmed by the XANES result (Fig. S5b) [59]. Moreover, the S L-edge XANES spectra and S 2p spectra for P*m*PDA-GR-Fe (Fig. S6) before and after acid leaching showed that the –C–S–C– covalent bond can be stable in the acid solution. According to previous studies, –C–S–C– is beneficial for enhancing the catalytic activity of ORR [60,61]. The high-resolution Fe 2p spectrum of P*m*PDA-GR-Fe (Fig. 3d) can be divided into three peaks for FeN_x (711.1 eV), FeS (724.03 eV), and Fe (708.1 eV) with a satellite peak at 716.8 eV [53]. The peak at 711.1 eV suggested the existence of Fe-N species which are active sites for ORR [28,62].

The ORR activity of P*m*PDA-GR-Fe was first evaluated in alkaline media. CV was carried out in O_2- and Ar-saturated 0.1 mol L^{-1} KOH using commercial Pt/C (20 wt%, Johnson Matthey). As shown in Fig. S7a, no obvious peak is observed in Ar-saturated 0.1 mol L^{-1} KOH electrolyte, while an obvious cathodic peak can be observed in O_2-saturated electrolyte, indicating that the P*m*PDA-GR-Fe catalyst is highly active toward ORR. The peak at 0.90 V from P*m*PDA-GR-Fe is much higher than that of Pt/C (0.83 V, Fig. S7b), suggesting excellent ORR activity of the P*m*PDA-GR-Fe catalyst. Meanwhile, as shown in Fig. 4a, the linear sweep voltammetric (LSV) curves confirm that P*m*PDA-GR-Fe exhibits prominent elec-

trocatalytic activity with an onset potential (E_{onset}) of ~1.02 V and a half-wave potential ($E_{1/2}$) of ~0.88 V. These values are higher than those of Pt/C tested under the same conditions (E_{onset} ~1.0 V and $E_{1/2}$ ~0.85 V). In contrast, the samples that directly pyrolyzed without iron adsorption or without using graphene as the template exhibited relatively poor performance (Fig. 4a), suggesting that both Fe and graphene are indispensable to achieve prominent ORR activity. Fig. 4b shows the Tafel plots of both P*m*PDA-GR-Fe and commercial Pt/C catalysts derived from Fig. 4a. The P*m*PDA-GR-Fe catalyst exhibits a Tafel slope of 67 mV dec^{-1} which is lower than that of the Pt/C catalyst (70 mV dec^{-1}), indicating P*m*PDA-GR-Fe has a good kinetic process for ORR. The average electron transfer number (n) calculated from the RRDE measurements (Fig. 4c) at all potentials is 3.98 which is close to the value calculated from the Koutechy-Levich (K-L) equation (n=4, Fig. S8), confirming the desired four-electron oxygen reduction pathway. RRDE results also showed that the H_2O_2 yield remained below 3.6% at all potentials and dropped to 0.7% at 0.8 V *vs.* RHE, indicating the P*m*PDA-GR-Fe catalyst has extremely high ORR catalytic efficiency. Moreover, the catalyst also showed high stability for ORR. The stability of P*m*PDA-GR-Fe and Pt/C catalysts were investigated at
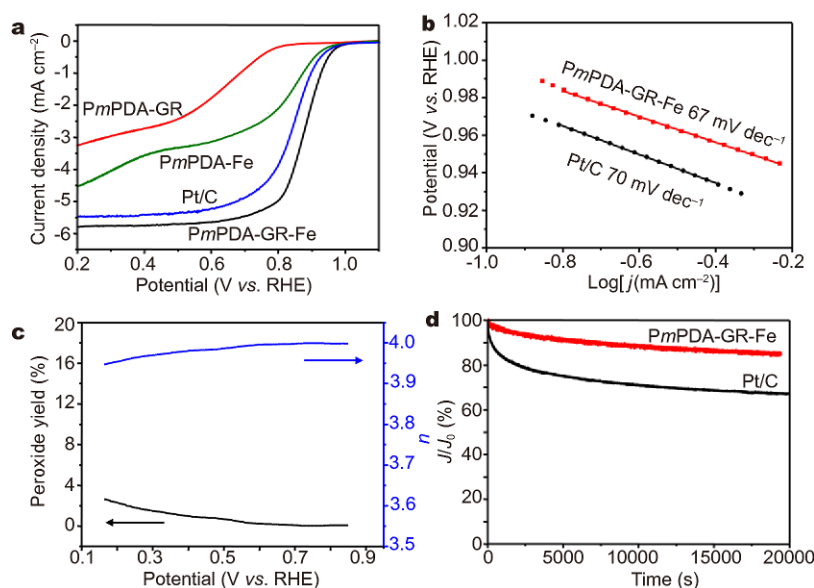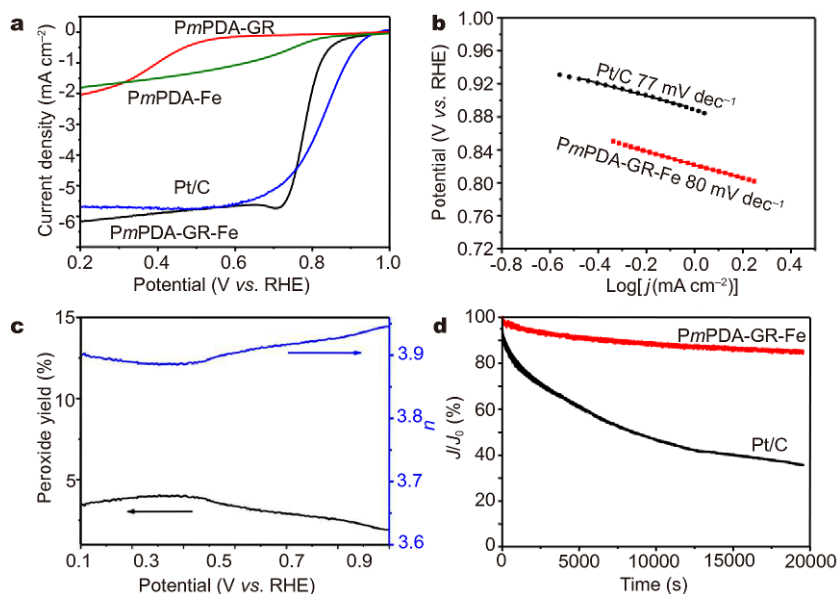
Figure 4 (a) LSV curves of PmPDA-GR, PmPDA-Fe, PmPDA-GR-Fe, and Pt/C in O_2-saturated 0.1 mol L^{-1} KOH. (b) Tafel plots obtained from the RDE measurements on PmPDA-GR-Fe and Pt/C catalysts. (c) The peroxide yield and the calculated electron transfer number of PmPDA-GR-Fe in O_2-saturated 0.1 mol L^{-1} KOH measured during ORR from RRDE tests. (d) Chronoamperometric responses of PmPDA-GR-Fe and Pt/C catalysts at 0.75 V. Electrode rotation speed, 1,600 rpm; scan rate, 10 mV s^{-1}.

0.75 V in O_2-saturated electrolyte for 20,000 s (Fig. 4d). About 86% of the original current density was retained for the PmPDA-GR-Fe catalyst, whereas Pt/C catalyst displayed a much higher current loss of ~33%, clearly indicating superior stability of the PmPDA-GR-Fe catalyst. Furthermore, after adding methanol to the electrolyte, no significant change was observed in the CV curve of PmPDA-GR-Fe (Fig. S9a), implying the newly synthesized catalyst was inert to the methanol crossover effect, while Pt/C was rather vulnerable to methanol (Fig. S9b). These results demonstrate that PmPDA-GR-Fe catalyst has much better selectivity and stability than the commercial Pt/C catalyst toward ORR in alkaline media.

To further investigate the potential application of PmPDA-GR-Fe catalyst in PEMFCs, ORR activity of the PmPDA-GR-Fe catalyst was examined in 0.1 mol L^{-1} HClO$_4$. CV curves in Fig. S10 reveal that the PmPDA-GR-Fe catalyst also possesses excellent ORR activity in acidic electrolytes. The peak potential at 0.75 V $vs.$ RHE of PmPDA-GR-Fe is very close to that of Pt/C (0.83 V). The LSV curves in Fig. 5a confirm that PmPDA-GR-Fe exhibits excellent ORR activity with E_{onset} of ~0.94 V $vs.$ RHE and $E_{1/2}$ of ~0.79 V $vs.$ RHE. These values are comparable to those of Pt/C tested under the same conditions (E_{onset} ~0.96V and $E_{1/2}$ ~0.83 V). In addition, the mass activity of PmPDA-GR-Fe catalyst was 10.8 A g^{-1} at 0.80 V, which is very competitive compared to previous studies (Table S1). Control experiments indicated that

both graphene and Fe were crucial to achieve such high ORR activity in acidic electrolytes (Fig. 5a). Accordingly, Tafel plots in Fig. 5b show that the PmPDA-GR-Fe catalyst has a Tafel slope of 80 mV dec^{-1} which is very close to that of the Pt/C catalyst (77 mV dec^{-1}). The average electron transfer number (n) calculated from the RRDE measurements at all potentials was 3.93, which confirmed the four-electron oxygen reduction process (Fig. 5c). RRDE results also showed that the H_2O_2 yield remained below 4.1% at all potentials and dropped to 1.9% at 0.8 V $vs.$ RHE, indicating the PmPDA-GR-Fe catalyst has excellent ORR catalytic efficiency even in acidic media. Moreover, parallel stability tests revealed that the PmPDA-GR-Fe catalyst possessed much higher stability and better methanol tolerance than Pt/C catalyst (Fig. 5d and S11), implying that PmPDA-GR-Fe is more stable than Pt/C toward PEMFC applications.

Obviously, the PmPDA-GR-Fe catalyst exhibits attractive ORR performance both in alkaline and acidic media, which is among the best reported ORR electrocatalysts that are active in both electrolytes (Table S2). Our control experiments confirmed that acid leaching was necessary to expose the catalytic sites by removing electrocatalytically inactive species (Fig. S12). Moreover, polyaniline (PANI) was used as the polymer precursor to form the PANI-GR-Fe catalyst, which was investigated under the same conditions. Electrocatalytic tests indicated that the catalyst prepared using PANI as the precursor

Figure 5 (a) LSV curves of P*m*PDA-GR, P*m*PDA-Fe, P*m*PDA-GR-Fe, and Pt/C in O_2-saturated 0.1 mol L^{-1} $HClO_4$. (b) Tafel plots obtained from the RDE measurements on P*m*PDA-GR-Fe and Pt/C catalysts. (c) The peroxide yield and the calculated electron transfer number of P*m*PDA-GR-Fe in O_2-saturated 0.1 mol L^{-1} $HClO_4$ during ORR measured from RRDE tests. (d) Chronoamperometric responses of P*m*PDA-GR-Fe and Pt/C catalysts at 0.7 V. Electrode rotation speed, 1,600 rpm; scan rate, 10 mV s^{-1}.

exhibited much inferior ORR performance (Fig. S13). Thus, P*m*PDA is indispensable to achieve the prominent ORR activity.

Subsequently, thiocyanate ion (SCN^-) poisoning experiments were carried out to determine whether M-N-C is the active species in ORR. SCN^- ions are known to strongly coordinate with metal ions to form stable complexes and hence poison the metal containing active sites in acidic conditions [28]. As shown in Fig. S14, the ORR activity of P*m*PDA-GR-Fe was remarkably declined after adding SCN^- into 0.1 mol L^{-1} $HClO_4$, indicating that Fe–N–C species are the primary active species for ORR. Meanwhile, to probe the possible S-doping on the catalytic activity of P*m*PDA-GR-Fe, the P*m*PDA-GO sample was washed more than 10 times to minimize the content of S in the sandwich-like carbon nanosheets while ensuring that the polymerization process was not affected. EA and ICP-MS were used to quantify the variation of each element in the final catalyst. The C, N, S, O and Fe contents in P*m*PDA-GR-Fe after thorough purification were 88.08, 5.05, 0.65, 4.24 and 1.27 wt%, respectively. The S content obviously decreased compared to the original P*m*PDA-GR-Fe catalyst. The reduction of the S content in the catalyst caused a dramatic loss in ORR activity (Fig. S15), though the chemical nature of each element was largely unchanged (Fig. S16). Therefore, the presence of S could be beneficial for enhancing ORR

activity [41,47,51]. Moreover, electrochemical impedance spectroscopy (EIS) (Fig. S17) revealed that the graphene-templated sandwich-like carbon nanosheets generally showed a much lower charge-transfer resistance than the control samples without graphene in both alkaline and acidic media, which could account for the observed prominent ORR activity of the P*m*PDA-GR-Fe catalyst. Furthermore, control experiments indicated that appropriate amounts of GO should be used to form the optimal sandwich-like structure (Fig. S18). Thus, the existence of multiple dopants, high surface area and unique sandwich-like structure with encapsulated conductive graphene sheets leads to the high-performance P*m*PDA-GR-Fe catalyst.

Based on the appealing ORR activity of the P*m*PDA-GR-Fe catalyst in electrochemical tests, we further carried out preliminary tests by using the P*m*PDA-GR-Fe as cathode catalyst both in a two-electrode zinc-air battery and a PEMFC. The open-circuit voltage (V_{OC}) of P*m*PDA-GR-Fe was 1.47 V with a peak power density of 280 mW cm^{-2}, surpassing the Pt/C cathode tested under the same conditions (1.45 V and 170 mW cm^{-2}, Fig. 6a). The specific capacity of the battery using P*m*PDA-GR-Fe as the cathode catalyst normalized to the mass of consumed Zn was 869 mA h g^{-1} at the discharge density of 50 mA cm^{-2} and 813 mA h g^{-1} at the discharge density of 100 mA cm^{-2} (Fig. S19), outperforming the battery as-
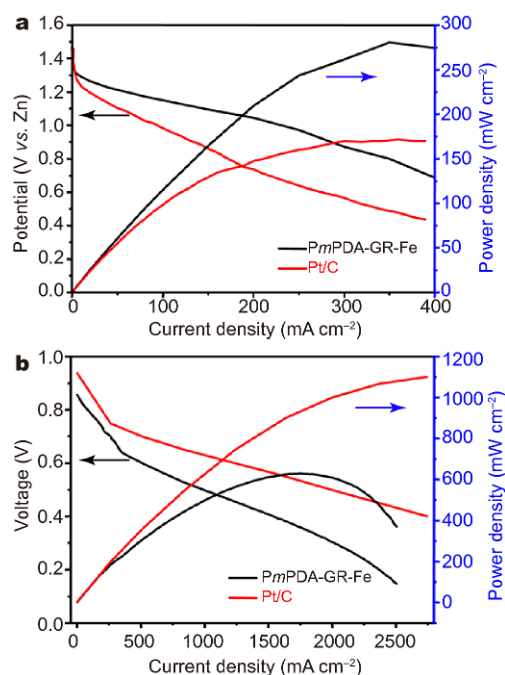
Figure 6 (a) Polarization and power density curves of the Zn–air battery assembled using P*m*PDA-GR-Fe and commercial Pt/C (20 wt%) as the cathode catalysts. (b) Polarization and power density curves of the PEMFC using P*m*PDA-GR-Fe and commercial Pt/C (60 wt%) as the cathode catalysts.

sembled with Pt/C at the same mass loading. On the other hand, Fig. 6b shows the fuel cell polarization curve and power density plot in the PEMFC using P*m*PDA-GR-Fe catalyst. The maximal power density can reach 630 mW cm^{-2} at cell voltage of 0.55 V and current density of 1,700 mA cm^{-2}. The performance is very competitive to the Pt/C catalyst. Note that these preliminary fuel cell results could be further improved after optimizing the MEA assembly and the fuel-cell testing conditions. These results strongly prove that the as-obtained P*m*PDA-GR-Fe catalyst holds great potential for applications in real electrochemical devices such as zinc-air batteries and fuel cells.

CONCLUSIONS

In conclusion, we successfully demonstrated a facile method to synthesize novel sandwich-like porous carbon nanosheets using graphene as the template. In this method, GO was introduced to build the sandwich-like structure with P*m*PDA coated on both sides of the GO surfaces *via in situ* polymerization. The P*m*PDA could coordinate with the Fe^{3+} ions to generate Fe–N active sites. Meanwhile, the introduced Fe could dramatically increase the specific surface area by forming removable nanoparticles during pyrolysis. Moreover, the S element

introduced during the polymerization process is beneficial for enhancing ORR activity. Thus, this approach could create a high density of active sites by formation of various dopants on the carbon layers. More importantly, the unique planar porous structure is helpful for exposing the active sites and mass transport. Furthermore, EIS results indicate that the encapsulated graphene could significantly reduce the charge transfer resistance. These attractive features enable the P*m*PDA-GR-Fe catalyst to exhibit excellent ORR activity in both alkaline and acidic media. We further showed that the P*m*PDA-GR-Fe catalyst can be successfully employed as a promising cathode catalyst both in Zn-air batteries and PEMFCs.

1   Han Y, Wang YG, Chen W, *et al.* Hollow N-doped carbon spheres with isolated cobalt single atomic sites: superior electrocatalysts for oxygen reduction. J Am Chem Soc, 2017, 139: 17269–17272

2   Chen Y, Ji S, Wang Y, *et al.* Isolated single iron atoms anchored on N-doped porous carbon as an efficient electrocatalyst for the oxygen reduction reaction. Angew Chem Int Ed, 2017, 56: 6937–6941

3   Cheng F, Chen J. Metal–air batteries: from oxygen reduction electrochemistry to cathode catalysts. Chem Soc Rev, 2012, 41: 2172–2192

4   Wang ZL, Xu D, Xu JJ, *et al.* Oxygen electrocatalysts in metal–air batteries: from aqueous to nonaqueous electrolytes. Chem Soc Rev, 2014, 43: 7746–7786

5   Li Y, Dai H. Recent advances in zinc–air batteries. Chem Soc Rev, 2014, 43: 5257–5275

6   Jiang WJ, Gu L, Li L, *et al.* Understanding the high activity of Fe–N–C electrocatalysts in oxygen reduction: Fe/Fe$_3$C nanoparticles boost the activity of Fe–N$_x$. J Am Chem Soc, 2016, 138: 3570–3578

7   Zhang G, Jin X, Li H, *et al.* N-doped crumpled graphene: bottom-up synthesis and its superior oxygen reduction performance. Sci China Mater, 2016, 59: 337–347

8   He D, Xiong Y, Yang J, *et al.* Nanocarbon-intercalated and Fe–N-codoped graphene as a highly active noble-metal-free bifunctional electrocatalyst for oxygen reduction and evolution. J Mater Chem A, 2017, 5: 1930–1934

9   Kuang M, Zheng G. Nanostructured bifunctional redox electrocatalysts. Small, 2016, 12: 5656–5675

10 Yu M, Zhou S, Liu Y, *et al.* Long life rechargeable Li-O$_2$ batteries enabled by enhanced charge transfer in nanocable-like Fe@N-doped carbon nanotube catalyst. Sci China Mater, 2017, 60: 415–426

11 Zhang Y, Huang LB, Jiang WJ, *et al.* Sodium chloride-assisted green synthesis of a 3D Fe–N–C hybrid as a highly active electrocatalyst for the oxygen reduction reaction. J Mater Chem A, 2016, 4: 7781–7787

12 Zhang J, Sasaki K, Sutter E, *et al.* Stabilization of platinum oxygen-reduction electrocatalysts using gold clusters. Science, 2007, 315: 220–222

13 Guan BY, Yu L, (David) Lou XW. A dual-metal–organic-framework derived electrocatalyst for oxygen reduction. Energy Environ

Sci, 2016, 9: 3092–3096

14 Zhao D, Shui JL, Chen C, et al. Iron imidazolate framework as precursor for electrocatalysts in polymer electrolyte membrane fuel cells. Chem Sci, 2012, 3: 3200–3205

15 Yan D, Li Y, Huo J, et al. Defect chemistry of nonprecious-metal electrocatalysts for oxygen reactions. Adv Mater, 2017, 29: 1606459

16 Meng F, Zhong H, Bao D, et al. In situ coupling of strung Co_4N and intertwined N–C fibers toward free-standing bifunctional cathode for robust, efficient, and flexible Zn–air batteries. J Am Chem Soc, 2016, 138: 10226–10231

17 Zhou T, Zhou Y, Ma R, et al. Achieving excellent activity and stability for oxygen reduction electrocatalysis by hollow meso-porous iron–nitrogen-doped graphitic carbon spheres. J Mater Chem A, 2017, 5: 12243–12251

18 Xiao M, Zhu J, Feng L, et al. Meso/macroporous nitrogen-doped carbon architectures with iron carbide encapsulated in graphitic layers as an efficient and robust catalyst for the oxygen reduction reaction in both acidic and alkaline solutions. Adv Mater, 2015, 27: 2521–2527

19 Zhang C, Wang YC, An B, et al. Networking pyrolyzed zeolitic imidazolate frameworks by carbon nanotubes improves con-ductivity and enhances oxygen-reduction performance in polymer-electrolyte-membrane fuel cells. Adv Mater, 2017, 29: 1604556

20 Zhou T, Du Y, Yin S, et al. Nitrogen-doped cobalt phosphate@nanocarbon hybrids for efficient electrocatalytic oxygen reduction. Energy Environ Sci, 2016, 9: 2563–2570

21 Li Y, Zhou W, Wang H, et al. An oxygen reduction electrocatalyst based on carbon nanotube–graphene complexes. Nat Nanotechnol, 2012, 7: 394–400

22 Liang Y, Li Y, Wang H, et al. Co_3O_4 nanocrystals on graphene as a synergistic catalyst for oxygen reduction reaction. Nat Mater, 2011, 10: 780–786

23 Yin P, Yao T, Wu Y, et al. Single cobalt atoms with precise N-coordination as superior oxygen reduction reaction catalysts. Angew Chem Int Ed, 2016, 55: 10800–10805

24 Liu J, Sun X, Song P, et al. High-performance oxygen reduction electrocatalysts based on cheap carbon black, nitrogen, and trace iron. Adv Mater, 2013, 25: 6879–6883

25 Ding Y, Niu Y, Yang J, et al. A metal-amino acid complex-derived bifunctional oxygen electrocatalyst for rechargeable zinc-air bat-teries. Small, 2016, 12: 5414–5421

26 Shang L, Yu H, Huang X, et al. Well-dispersed ZIF-derived Co,N-Co-doped carbon nanoframes through mesoporous-silica-pro-tected calcination as efficient oxygen reduction electrocatalysts. Adv Mater, 2016, 28: 1668–1674

27 Meng FL, Wang ZL, Zhong HX, et al. Reactive multifunctional template-induced preparation of Fe-N-doped mesoporous carbon microspheres towards highly efficient electrocatalysts for oxygen reduction. Adv Mater, 2016, 28: 7948–7955

28 Wang Q, Zhou ZY, Lai YJ, et al. Phenylenediamine-based FeN_x /C catalyst with high activity for oxygen reduction in acid medium and its active-site probing. J Am Chem Soc, 2014, 136: 10882–10885

29 Zhou R, Qiao SZ. An Fe/N co-doped graphitic carbon bulb for high-performance oxygen reduction reaction. Chem Commun, 2015, 51: 7516–7519

30 Xia W, Mahmood A, Liang Z, et al. Earth-abundant nanomaterials for oxygen reduction. Angew Chem Int Ed, 2016, 55: 2650–2676

31 Li J, Ghoshal S, Liang W, et al. Structural and mechanistic basis for the high activity of Fe–N–C catalysts toward oxygen reduction.

Energy Environ Sci, 2016, 9: 2418–2432

32 Yang J, Wang X, Li B, et al. Novel iron/cobalt-containing poly-pyrrole hydrogel-derived trifunctional electrocatalyst for self-powered overall water splitting. Adv Funct Mater, 2017, 27: 1606497

33 Nie Y, Li L, Wei Z. Recent advancements in Pt and Pt-free catalysts for oxygen reduction reaction. Chem Soc Rev, 2015, 44: 2168–2201

34 Wang W, Chen W, Miao P, et al. NaCl crystallites as dual-func-tional and water-removable templates to synthesize a three-di-mensional graphene-like macroporous Fe-N-C catalyst. ACS Catal, 2017, 7: 6144–6149

35 Gao W, Havas D, Gupta S, et al. Is reduced graphene oxide fa-vorable for nonprecious metal oxygen-reduction catalysts? Carbon, 2016, 102: 346–356

36 Wu G, More KL, Xu P, et al. A carbon-nanotube-supported gra-phene-rich non-precious metal oxygen reduction catalyst with enhanced performance durability. Chem Commun, 2013, 49: 3291–3293

37 Li Q, Pan H, Higgins D, et al. Metal-organic framework-derived bamboo-like nitrogen-doped graphene tubes as an active matrix for hybrid oxygen-reduction electrocatalysts. Small, 2015, 11: 1443–1452

38 Jaouen F, Herranz J, Lefevre M, et al. Cross-laboratory experi-mental study of non-noble-metal electrocatalysts for the oxygen reduction reaction. ACS Appl Mater Interfaces, 2009, 1: 1623–1639

39 Zhong H, Wang J, Zhang Y, et al. ZIF-8 Derived Graphene-Based Nitrogen-Doped Porous Carbon Sheets as Highly Efficient and Durable Oxygen Reduction Electrocatalysts. Angew Chem Int Ed, 2014, 53: 14235–14239

40 Xiang Z, Xue Y, Cao D, et al. Highly efficient electrocatalysts for oxygen reduction based on 2D covalent organic polymers com-plexed with non-precious metals. Angew Chem Int Ed, 2014, 53: 2433–2437

41 Zhang P, Sun F, Xiang Z, et al. ZIF-derived in situ nitrogen-doped porous carbons as efficient metal-free electrocatalysts for oxygen reduction reaction. Energy Environ Sci, 2014, 7: 442–450

42 Yang T, Liu J, Zhou R, et al. N-doped mesoporous carbon spheres as the oxygen reduction reaction catalysts. J Mater Chem A, 2014, 2: 18139–18146

43 Liang HW, Wei W, Wu ZS, et al. Mesoporous metal–nitrogen-doped carbon electrocatalysts for highly efficient oxygen reduction reaction. J Am Chem Soc, 2013, 135: 16002–16005

44 Qu K, Zheng Y, Dai S, et al. Polydopamine–graphene oxide de-rived mesoporous carbon nanosheets for enhanced oxygen re-duction. Nanoscale, 2015, 7: 12598–12605

45 Xia BY, Yan Y, Wang X, et al. Recent progress on graphene-based hybrid electrocatalysts. Mater Horiz, 2014, 1: 379–399

46 Li S, Wu D, Cheng C, et al. Polyaniline-coupled multifunctional 2D metal oxide/hydroxide graphene nanohybrids. Angew Chem Int Ed, 2013, 52: 12105–12109

47 Qiao M, Tang C, He G, et al. Graphene/nitrogen-doped porous carbon sandwiches for the metal-free oxygen reduction reaction: conductivity versus active sites. J Mater Chem A, 2016, 4: 12658–12666

48 Li S, Wu D, Liang H, et al. Metal-nitrogen doping of mesoporous carbon/graphene nanosheets by self-templating for oxygen reduc-tion electrocatalysts. ChemSusChem, 2014, 7: 3002–3006

49 Yan J, Yang L, Lin MF, et al. Polydopamine spheres as active templates for convenient synthesis of various nanostructures. Small, 2013, 9: 596–603

50　Fu X, Zamani P, Choi JY, *et al. In situ* polymer graphenization ingrained with nanoporosity in a nitrogenous electrocatalyst boosting the performance of polymer-electrolyte-membrane fuel cells. Adv Mater, 2017, 29: 1604456

51　Wen Z, Ci S, Hou Y, *et al.* Facile one-pot, one-step synthesis of a carbon nanoarchitecture for an advanced multifunctonal electrocatalyst. Angew Chem Int Ed, 2014, 53: 6496–6500

52　Xu C, Zeng Y, Rui X, *et al.* Controlled soft-template synthesis of ultrathin C@FeS nanosheets with high-li-storage performance. ACS Nano, 2012, 6: 4713–4721

53　Zhu Y, Zhang B, Liu X, *et al.* Unravelling the structure of electrocatalytically active Fe-N complexes in carbon for the oxygen reduction reaction. Angew Chem Int Ed, 2014, 53: 10673–10677

54　Hu Y, Jensen JO, Zhang W, *et al.* Hollow spheres of iron carbide nanoparticles encased in graphitic layers as oxygen reduction catalysts. Angew Chem Int Ed, 2014, 53: 3675–3679

55　Wang YC, Lai YJ, Song L, *et al.* S-doping of an Fe/N/C ORR catalyst for polymer electrolyte membrane fuel cells with high power density. Angew Chem, 2015, 127: 10045–10048

56　Zhang LS, Liang XQ, Song WG, *et al.* Identification of the nitrogen species on N-doped graphene layers and Pt/NG composite catalyst for direct methanol fuel cell. Phys Chem Chem Phys, 2010, 12: 12055–12059

57　Wu ZS, Chen L, Liu J, *et al.* High-performance electrocatalysts for oxygen reduction derived from cobalt porphyrin-based conjugated mesoporous polymers. Adv Mater, 2014, 26: 1450–1455

58　Yang Z, Yao Z, Li G, *et al.* Sulfur-doped graphene as an efficient metal-free cathode catalyst for oxygen reduction. ACS Nano, 2012, 6: 205–211

59　Sarret G, Connan J, Kasrai M, *et al.* Chemical forms of sulfur in geological and archeological asphaltenes from Middle East, France, and Spain determined by sulfur K- and L-edge X-ray absorption near-edge structure spectroscopy. GeoChim CosmoChim Acta, 1999, 63: 3767–3779

60　Wang X, Wang J, Wang D, *et al.* One-pot synthesis of nitrogen and sulfur co-doped graphene as efficient metal-free electrocatalysts for the oxygen reduction reaction. Chem Commun, 2014, 50: 4839–4842

61　Shen H, Gracia-Espino E, Ma J, *et al.* Synergistic effects between atomically dispersed Fe−N−C and C−S−C for the oxygen reduction reaction in acidic media. Angew Chem, 2017, 129: 13988–13992

62　Wu G, Chen Z, Artyushkova K, et al. Polyaniline-derived non-precious catalyst for the polymer electrolyte fuel cell cathode. ECS Trans, 2008, 16: 159–170

Author contributions　Xu H and Wang T conceived and designed the research. Wang T, Wang J, Wang X, Yang J performed the experiments. Wang T, Yang J, Wang X, Yang J, Liu J and Xu H participated in the interpretation of experimental results. All authors participated in the general discussion.

Conflict of interest　The authors declare no conflict of interest.

Supplementary information　Experimental details are available in the online version of the paper.

Tao Wang received his BSc degree from Hefei University of Technology in 2015. He is currently a PhD candidate in the Department of Polymer Science and Engineering, University of Science and Technology of China. His current research is developing functional polymers for flexible energy devices.

CELEBRATE DIVERSITY

Jianguo Liu received his PhD degree from Dalian Institute of Chemical Physics in China. Then he worked as post-doc in Hong Kong University of Science and Technology and University of Newcastle upon Tyne in UK. He joined Nanjing University as an associate professor in 2007, and become a professor in 2013. His research now focuses on fuel cells and Li-ion batteries.

Hangxun Xu received his BSc degree from University of Science and Technology of China and PhD in Materials Chemistry from the University of Illinois at Urbana-Champaign. Thereafter, he was a Postdoctoral Research Associate with Prof. John Rogers. He came back to the USTC as a Professor in 2013 through the "National 1000 Young Talents" program. His current research focuses on developing functional polymers for applications in energy conversion and flexible electronics.

石墨烯模板法制备类似三明治结构的多孔碳纳米片用于高效催化酸/碱性条件下氧还原反应的研究

汪韬[1]，王健宇[2]，王绪[1]，杨佳[1]，刘建国[2*]，徐航勋[1*]

摘要 开发低成本, 高性能氧还原反应(ORR)电催化剂对于燃料电池和金属空气电池的规模化应用至关重要. 基于石墨烯的碳催化剂已经被广泛用于碱性电解质中的ORR. 然而, 与Pt/C催化剂相比, 石墨烯基催化剂在酸性电解质中的性能仍然需要进一步提升. 在这个工作中, 我们发展了一种非常高效的模板方法来制备基于石墨烯的具有三明治结构的多孔碳纳米片电催化剂, 其在碱性和酸性电解质中均具有非常好的ORR催化性能. 首先, 被氧化石墨烯吸附的苯二胺分子通过氧化聚合形成富氮聚合物网络, 接着铁(Fe)盐被吸附到聚合物网络中, 并且在热解之后形成ORR活性位点Fe–N–C以及Fe, FeS和FeN$_{0.05}$纳米颗粒, 最终得到类似三明治结构的碳纳米片ORR电催化剂. 由于这种结构中存在较高密度的ORR活性位点, 所获得的催化剂显示出非常高效的ORR活性, 在0.1 mol L^{-1} KOH中半波电位比Pt/C高30 mV. 更重要的是, 在0.1 mol L^{-1} HClO$_4$中, 催化剂的半波电位仅比Pt/C低约40 mV. 这种独特的平面三明治结构可以在催化反应中暴露出丰富的ORR活性位点, 同时, 石墨烯层和多孔结构可以提高电导率以及促进传质, 这两者对于实现高活性ORR催化至关重要. 在碱性和酸性条件中, 突出的电催化活性和耐久性表明这些碳纳米片作为贵金属基ORR催化剂的替代物具有很大的潜力, 优秀的锌空气电池和质子交换膜燃料电池性能直接证实这种材料在实际电化学能源转化装置中也非常有应用前景.